

Photophysical properties of Kuratowski-type coordination compounds $[\text{M}^{\text{II}}\text{Zn}_4\text{Cl}_4(\text{Me}_2\text{bta})_6]$ ($\text{M}^{\text{II}} = \text{Zn}$ or Ru) featuring long-lived excited electronic states[†]

Ying-Ya Liu,^a Maciej Grzywa,^a Markus Tonigold,^a German Sastre,^{*b} Tanja Schüttrigkeit,^c Nicholas S. Leeson^d and Dirk Volkmer^{*a,e}

The syntheses of Kuratowski-type pentanuclear clusters featuring $\{\text{MZn}_4\text{Cl}_4\}$ cores ($\text{M}^{\text{II}} = \text{Ru}$ or Zn) that incorporate triazolate ligands are described. The coordination compounds are characterized by single-crystal X-ray diffraction, X-ray powder diffraction (XRD), FTIR- and UV-vis spectroscopy. $[\text{Ru}^{\text{II}}\text{Zn}_4\text{Cl}_4(\text{Me}_2\text{bta})_6]\cdot 2\text{DMF}$ ($\text{Me}_2\text{bta}^- = 5,6\text{-dimethyl-1,2,3-benzotriazolate}$) (**1**) crystallizes in the cubic system, while $[\text{Zn}_5\text{Cl}_4(\text{ta})_6]$ ($\text{ta}^- = 1,2,3\text{-triazolate}$) (**3**) crystallizes in the tetragonal system. Both compounds feature structurally similar cluster topologies in which the central octahedrally coordinated metal ion is coordinated to six triazolate ligands. Each triazolate ligand is coordinated with two zinc ions (μ_3 -bridging mode), leading altogether to a pentanuclear cluster of T_d point group symmetry. Photophysical investigations reveal that compound $[\text{Zn}_5\text{Cl}_4(\text{Me}_2\text{bta})_6]\cdot 2\text{DMF}$ (**2**) shows a short-lived excited electronic state, which can be populated with high quantum yield. The isostructural compound $[\text{Ru}^{\text{II}}\text{Zn}_4\text{Cl}_4(\text{Me}_2\text{bta})_6]\cdot 2\text{DMF}$ (**1**), on the other hand, shows a long-lived photoexcited state, owing to an internal singlet to triplet conversion of the electronic states, as revealed by time-resolved fluorescence spectroscopy. Insights gained from these studies open up novel design strategies towards photocatalytically active metal–organic frameworks incorporating photoactive Kuratowski-type secondary building units such as MFU-4 (Metal–Organic Framework Ulm University-4).

Introduction

Triazole ligands and their derivatives have been widely used to build up multinuclear metal complexes.^{1–3} They have witnessed widespread applications in transition metal complexes, particularly in spin cross-over complexes,¹ mixed-valence complexes^{4,5} and structural models for metallo-enzymes.^{6–8} Previous studies

have demonstrated that 1,2,3-triazoles have an azo character, while 1,2,4-triazoles have an azine character.^{9,10} Triazole molecules are aromatic molecules that behave as electron donors with the HOMO energy being higher for 1,2,4-triazolate compared to 1,2,3-triazolate. Their physical properties such as dipole moment and melting point are markedly different with higher values for 1,2,4-triazolate (3.17 D and 121 °C) than 1,2,3-triazolate (1.77 D and 23 °C), respectively.¹¹ The different positions of the nitrogen atoms in both the heterocyclic ring systems lead to different coordination modes in the (transition) metal coordination compounds, of which complexes containing 1,2,3-triazolate ligands are much less widely explored in comparison to their 1,2,4-triazolate-based counterparts. Among many coordination compounds, ruthenium or rhenium complexes containing either type of triazole ligands have been studied for their unique redox and photophysical properties.^{12–18}

Based on 1,2,3-triazolate ligands we have recently reported on a compound library for which we have coined the term “Kuratowski-type” coordination compounds.^{19,20} These complexes have a particular structural feature in common: the fundamental coordination unit shows a central metal ion coordinated by six triazolate ligands spanning a Cartesian system, which can be assembled either into discrete pentanuclear coordination compounds^{21–25} or into 3D porous cubic frameworks (Fig. 1).^{26,27}

^aUlm University, Institute of Inorganic Chemistry II - Materials and Catalysis, Albert-Einstein-Allee 11, D-8908, Ulm, Germany

^bInstituto de Tecnología Química (UPV-CSIC), Universidad Politécnica de Valencia, Av. Los Naranjos s/n, 46022, Valencia, Spain

^cHamamatsu Photonics Deutschland GmbH, Arzbergerstraße 10, D-82211, Herrsching, Germany

^dEdinburgh Instruments Ltd, 2 Bain Square, Kirkton Campus, Livingston, UK, EH54 7DQ

^eAugsburg University, Institute of Physics, Chair of Solid State and Material Science, Universitätsstr. 1, D-86159, Augsburg, Germany. E-mail: dirk.volkmer@physik.uni-augsburg.de; Fax: +49 (821) 598-5955; Tel: +49 (821) 598-3006

[†]Electronic supplementary information (ESI) available: ¹H-NMR of mixture **1a**, LIFDI-MS spectrum of compound **1** and molecular ion peak, XRD patterns, SEM and optic microscopic graph of both compounds, analysis of bands from TDFT calculations, calculated UV-Vis, infrared and Raman spectra, detailed spectroscopic analysis of all compounds. CCDC reference numbers 804602 and 804603. For ESI and crystallographic data in CIF or other electronic format see DOI: 10.1039/c0dt01750g

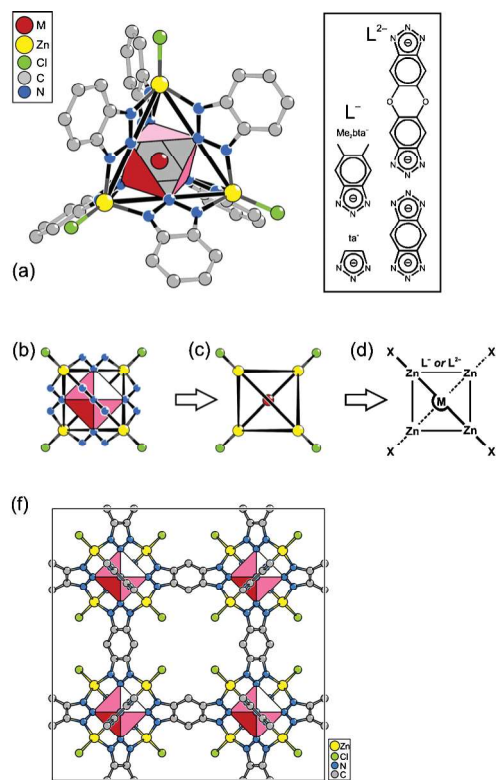


Fig. 1 (a) Structural formulas of Kuratowski-type coordination compounds: monoanionic 1,2,3-triazolate ligands ($L^- = ta^-$ or Me_2bta^-) lead to discrete coordination complexes $[M^n Zn_4 Cl_4 (L_6)]$, whereas cubic porous frameworks $[M^n Zn_4 Cl_4 (L_3)]$ (e.g. MFU-4l (f) ²⁶) are constructed from bis-triazolate ligands L^{2-} . (b-d) Derivation of a skeletal formula representing the connectivity of the $[M^n Zn_4 Cl_4 (L_6)]$ units.

The graph theoretical analysis proves that the $[M^n Zn_4 Cl_4 (L_6)]$ units contain the nonplanar $K_{3,3}$ graph. According to a theorem of C. Kuratowski,²⁸ a finite graph is planar if - and only if - it does not contain a subgraph that is a subdivision of K_5 (the complete graph on five vertices) or $K_{3,3}$ (complete bipartite graph on six vertices, three of which connect to each of the other three). As can be seen in Fig. 2 the molecular graph of $[M^n Zn_4 Cl_4 (L_6)]$ units in fact contains a subgraph of $K_{3,3}$. Accordingly there is no way to draw $[M^n Zn_4 Cl_4 (L_6)]$ as a planar graph and thus we propose a pseudo-perspective skeletal formula as derived in Fig. 1 (b-d) to represent Kuratowski-type coordination compounds here and for the future.

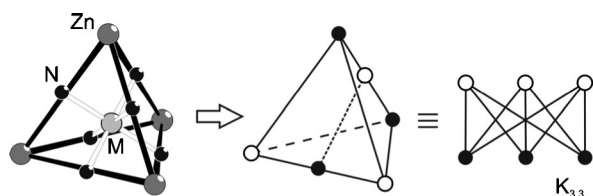


Fig. 2 Formal derivation of the $K_{3,3}$ graph, which can be used to represent the connectivity scheme in Kuratowski-type coordination compounds.

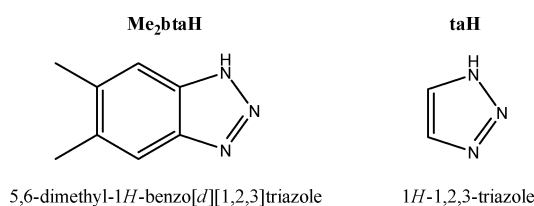
In previous work we have reported on the synthesis of Kuratowski-type coordination compounds $[M^n Zn_4 Cl_4 (Me_2bta)_6]$

with $M^{II} = Zn^{II}$ or Co^{II} ($Me_2btaH = 5,6$ -dimethyl-1,2,3-benzotriazole).²⁰ The series of isostructural compounds featuring open-shell 3d-metal centres in the central octahedral site of the pentanuclear units was recently extended *via* synthesis and characterization of their $Fe(II)$, $Ni(II)$, and $Cu(II)$ counterparts.¹⁹ It should be noted here, that structurally similar homopentanuclear complexes were previously reported;^{23,24,25} their systematic development with respect to catalytic applications, and their use as rigid building blocks in supramolecular coordination compounds,^{29,30} or infinite 3D coordination networks,^{26,27,31} however, constitutes a recent finding, the potential of which shall be fully exploited in the future.

Since Kuratowski-type coordination units feature a unique combination of redox-active and Lewis-acidic metal centres, interesting bifunctional catalytic properties might arise. The focus of the present studies thus was laid upon the synthesis of the novel Kuratowski-type compound $[Ru^{II} Zn_4 Cl_4 (Me_2bta)_6] \cdot 2DMF$ (**1**), in which $Ru(II)$ centres are introduced in the central octahedral site. Doing so, useful photophysical properties might be added to this coordination unit, such as a long-lived excited electronic state upon irradiation. In the present publication we will, therefore, report the synthesis of compound **1**, its solid state structure as well as its photophysical characteristics, investigated by means of fluorescence spectroscopy and lifetime studies. The previously described $[Zn_5 Cl_4 (Me_2bta)_6] \cdot 2DMF$ (**2**)²⁰ will be considered as reference and compared to the Ru analogue.

In addition, compound $[Zn_5 Cl_4 (ta)_6]$ (**3**), which is a structural analogue of (**2**), was synthesized employing 1,2,3-triazolate as the ligand, in order to assess the electronic nature of the ligand on the spectroscopic properties of the coordination compounds, and to adjust the basis sets and exchange functional in the DFT calculations to the desired levels of accuracy.

The structural, spectroscopic and photophysical properties of all the Kuratowski-type coordination units described here are compared to theoretical models gleaned from density functional theory (DFT) calculations. Time dependent DFT³² (TDDFT) is used in order to provide a detailed account of the photoelectronic properties of the title compounds. The TDDFT method including an appropriate choice of functionals has shown widespread application due to its good compromise between accuracy and computational cost. The modelling of (**3**), with fewer atoms than (**1**) and (**2**), will allow the testing of different functionals and basis sets at affordable computational costs, in order to compare computational with experimental results; and in this line of thought, calculations on the ligand molecules (Scheme 1) will be performed also as a means of calibration tests for the computational methodology.



Scheme 1 Structure diagrams of the 1,2,3-triazole ligands used in this work.

Results and discussion

Synthesis and characterization

Since initial attempts to prepare the desired $[\text{Ru}^{\text{II}}\text{Zn}_4\text{Cl}_4(\text{Me}_2\text{bta})_6]\cdot 2\text{DMF}$ compound *via* a conventional solvothermal route (starting from a stoichiometric mixture of $[\text{Ru}^{\text{II}}(\text{DMSO})_4\text{Cl}_2]$,³³ zinc chloride and Me_2btaH) failed, we developed a different synthetic approach. As summarized in Scheme 2, two novel routes were devised: In a multi-step synthesis (method 1), the first step starts from $[\text{Ru}^{\text{II}}\text{Cl}_2(\text{DMSO})_4]$, which is dissolved in a melt of Me_2btaH , leading to a ruthenium precursor complex, to which we tentatively assign the formula $[\text{Ru}^{\text{II}}(\text{Me}_2\text{btaH})_6]\text{Cl}_2$. According to previous studies,³³ a complete replacement of the coordinated DMSO with *N*-heterocyclic ligands is observed only when the complex is refluxed in the (solvent-free) neat ligand. Here we have used a large excess of ligand to ensure full ligand exchange. In the second step, compound **1** was synthesized by adding zinc chloride to react with the Ru precursor complex $[\text{Ru}^{\text{II}}(\text{Me}_2\text{btaH})_6]\text{Cl}_2$ under solvothermal conditions. In synthesizing compound **1**, the most difficult step was to separate the Ru precursor from impurities that, according to $^1\text{H-NMR}$ data (Fig. S1, ESI†), most likely consist of Ru compounds with fewer than six coordinated Me_2bta ligands. All efforts to isolate the putative precursor $[\text{Ru}^{\text{II}}(\text{Me}_2\text{btaH})_6]\text{Cl}_2$ in a pure state through column chromatography were unsuccessful. However, when a DMF solution of zinc chloride was added to the precursor, compound **1** was formed at moderate yield. Pure compound **1** precipitated from solution, the green–yellow single crystals showing a characteristic octahedral shape (Fig. S2, ESI†). By this method, crystals suitable for single-crystal X-ray structure analysis of $[\text{Ru}^{\text{II}}\text{Zn}_4\text{Cl}_4(\text{Me}_2\text{bta})_6]\cdot (\text{DMF})_2$ (**1**) were obtained directly. The presence of DMF molecules, which are occluded in the crystal lattice, is confirmed by elemental analysis and $^1\text{H-NMR}$ investigations. The experimental XRPD pattern is consistent with a theoretical pattern as calculated from the single crystal structural data, thus confirming the phase purity of **1** (Fig. S3, ESI†). The relative elemental ratio was examined by inductively coupled plasma atomic emission spectroscopy (ICP-AES), showing an approximate Ru:Zn molar ratio of 1:4, in good agreement to its molecular formula. The correct composition of **1** was further confirmed by mass spectroscopic

investigations employing a special ionization technique (LIFDI, Liquid Injection Field Desorption/Ionization). The LIFDI-MS spectrum in fact shows a base peak at m/z 1381.9, which is assigned to $[\text{RuZn}_4\text{Cl}_4(\text{C}_8\text{H}_8\text{N}_3)_6] (= [\text{1} - 2\text{DMF}])$. Moreover, the spectrum does not show any trace of $[\text{Zn}_5\text{Cl}_4(\text{C}_8\text{H}_8\text{N}_3)_6] (= [\text{2} - 2\text{DMF}])$ further confirming the purity of compound **1** (Fig. S4 and S5, ESI†).

Since the above described synthesis relies on a ruthenium precursor compound of putative composition, an alternative route was attempted by choosing a well-defined ruthenium complex $[\text{Ru}^{\text{II}}(\text{MeCN})_6][\text{ZnCl}_4]\cdot 2.5\text{H}_2\text{O}$ as the starting material,³⁴ which contains six weakly-coordinated acetonitrile ligands. A simple reaction of this Ru complex, ZnCl_2 and Me_2btaH in a stoichiometric ratio in DMF solution leads to the direct synthesis of the green–yellow crystalline compound **1** in approx. 16% yield. The phase purity of the compound once again was confirmed by ICP-AES, LIFDI-MS, $^1\text{H-NMR}$ and XRPD characterization (Fig. S3, ESI†).

In addition, compound **2** $[\text{Zn}_5\text{Cl}_4(\text{Me}_2\text{bta})_6]\cdot 2\text{DMF}$ was prepared as a reference sample for photophysical and computational studies, following a synthesis reported previously by our group.²⁰ The same pentanuclear $\{\text{Zn}_5\text{Cl}_4\}$ core is found in compound **3**, for the synthesis of which the conditions are much more flexible, and both the solvothermal reaction and microwave assisted synthesis yield the pure colourless crystalline product directly (Fig. S6, ESI†).

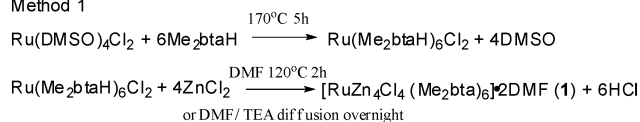
A single-crystal X-ray structure analysis of compound **3** has been accomplished, and experimental XRPD patterns are consistent with the simulated ones as gleaned from the corresponding single crystal structural data, thus confirming the phase purity of compound **3** (Fig. S7, ESI†).

Thermogravimetric (TG) analysis reveals that compound **1** exhibits a first weight loss of about 9.53% in the temperature range between 214–301 °C corresponding to the release of two DMF molecules per formula unit (calcd: 9.56%). The onset of the first weight loss step for compound **3**, in contrast, starts at 340 °C, which shows that **3** is thermally stable since it does not contain occluded solvent molecules.

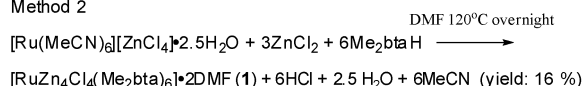
Compounds **1** and **3** are both insoluble in most common organic solvents, the former, however, is sparingly soluble in *N*-methyl-2-pyrrolidone (NMP), bromobenzene, or ethyl acetate.

Compound 1

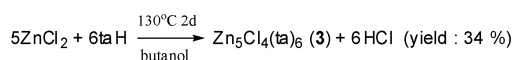
Method 1



Method 2



Compound 3 (method 1)



Scheme 2 Chemical equations for the preparation of compounds **1** and **3**.

Single-crystal structure analyses

The single-crystal X-ray structural analyses reveal the structurally similar pentanuclear coordination units of compounds **1** and **3** (Table 1). Compound **1** is isostructural with **2** and with a previously described series of heteropentanuclear compounds.^{19,20} As depicted in Fig. 1, compounds **1** and **3** both display a T_d symmetric Kuratowski-type coordination unit, in which the central metal ion (Ru^{2+} in compound **1** and Zn^{2+} in compound **3**, respectively) is octahedrally coordinated by six tridentate triazolate ligands (Me_2bta^- in compound **1** and ta^- in compound **3**, respectively) *via* their N donor atoms. The triazolate ligands span the edges of an imaginary tetrahedron thus providing four coordination sites at the corners of the tetrahedron, which are then filled by four zinc ions. The coordination shell of the latter is completed by chloride anions.

Table 1 Crystal data and structure refinement summary for compounds **1** and **3**

Compound	1	3
Empirical formula	RuZn ₄ Cl ₄ (C ₈ H ₈ N ₃) ₆ ·2C ₃ H ₇ NO	Zn ₅ Cl ₄ (C ₂ H ₂ N ₃) ₆
Formula	C ₅₄ H ₆₂ Cl ₄ N ₃₀ O ₂ RuZn ₄	C ₁₂ H ₁₂ Cl ₄ N ₁₈ Zn ₅
M _r	1527.59	877.04
T/K	293(2)	220(2)
Crystal system	Cubic	Tetragonal
Space group (no.)	<i>Fd</i> $\bar{3}$ <i>m</i> (no. 227)	<i>I</i> ₄ / <i>a</i> (no. 88)
<i>a</i> /Å	23.374(3)	14.937(3)
<i>c</i> /Å	23.374(3)	12.059(3)
<i>V</i> /Å ³	12770(3)	2690.5(10)
<i>Z</i>	8	4
<i>D_c</i> /g cm ⁻³	1.590	2.165
μ /mm ⁻¹	1.936	4.833
<i>F</i> (000)	6192	1712
θ Range/°	2.5–25.9	2.17–25.80
Refln total	24435	13772
Refln unique	646	1300
Refln obs.	556	1113
<i>R</i> _{int}	0.0606	0.0523
<i>R</i> ₁ (<i>I</i> > 2σ(<i>I</i>)) ^a	0.0236	0.0225
<i>wR</i> ₂ (all data) ^b	0.0600	0.0495
GooF	1.026	1.048
Largest diff. peak and hole/Å ⁻³	0.30 and –0.31	0.44 and –0.34

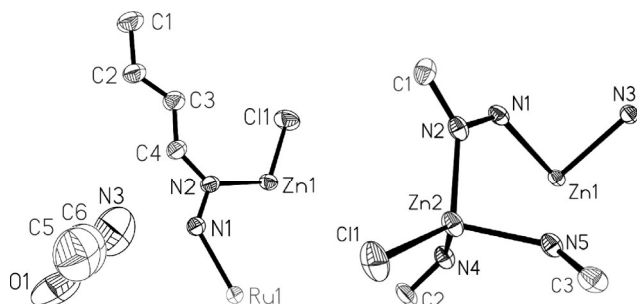
^a $R_1 = \sum |F_o| - |F_c| / \sum |F_o|$; ^b $wR_2 = \sum [w(F_o^2 - F_c^2)^2] / \sum [w(F_o^2)^2]^{1/2}$.

Table 2 Selected bond lengths (Å) and angles (°) of compounds **1** and **3**

Compound 1			
Ru1–N1	2.116(3)	Zn1–N2	2.000(2)
Zn1–Cl1	2.1649(8)	N1–N2	1.335(3)
N2–Zn1–N2 ^a	96.80(7)		
Compound 3			
Zn1–N1	2.169(2)	Zn1–N3	2.175(2)
Zn2–N2	2.025(2)	Zn2–N4	2.030(2)
Zn2–N5	2.028(2)	N1–N2	1.334(2)
N1–Zn1–N1 ^b	180.00	N1–Zn1–N3 ^b	90.79(6)
N3–Zn1–N3 ^b	90.011(2)	N3–Zn1–N3 ^c	178.42(12)
N1–Zn1–N3	89.21(6)	N2–Zn2–N4	98.25(8)
N2–Zn2–N5	100.27(8)	N4–Zn2–N5	98.88(8)

Symmetry transformations used to generate equivalent atoms for compound **1**:^a *y*, *z*, *x*; for compound **3**:^b *y* – 1/4, –*x* + 5/4, –*z* + 1/4; ^c –*x* + 1, –*y* + 3/2, *z* + 0

ORTEP plots of the asymmetric units of compounds **1** and **3** are shown in Fig. 3. Selected geometric parameters for both structures are presented in Table 2.

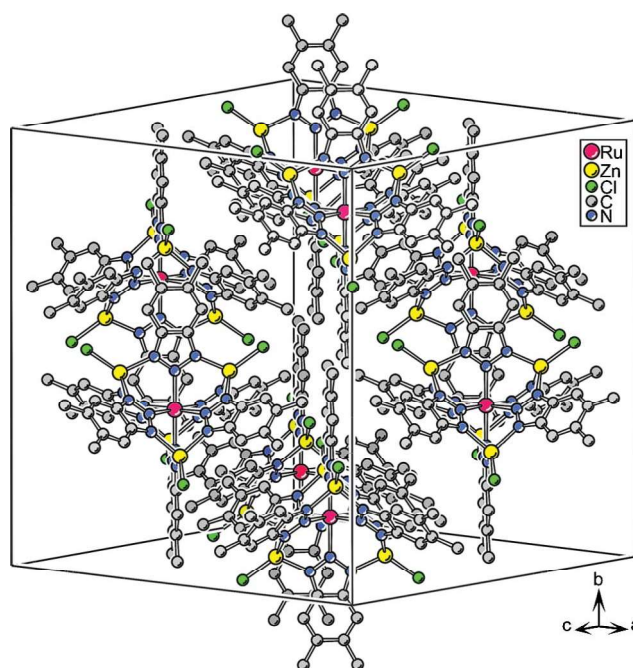
**Fig. 3** ORTEP plots of the asymmetric units of compound **1** (left) and **3** (right). The thermal ellipsoids are drawn at the 50% probability level. Hydrogen atoms are omitted for clarity.

Similar to compound **2**, compound **1** crystallizes in the cubic space group *Fd* $\bar{3}$ *m*, whereas compound **3** crystallizes in the tetragonal space group *I*₄/*a*. The crystal structures of compounds **1** and **3** show significantly different bond lengths between atoms at structurally equivalent positions. These are presumably due to differences in the electronic nature of the coordinating ligands (benzotriazolate as opposed to triazolate) and to different covalent radii of the metal ions in the central octahedral coordination site (Ru²⁺ as opposed to Zn²⁺).

Averaging the individual values for equivalent positions, the following geometrical data are obtained.

In compound **1**, the Ru–N bond distance is 2.116(3) Å, in good agreement with Ru–N bonds reported for structurally related Ru complexes.^{5,35} In compound **3**, the Zn1–N bond lengths vary from 2.169(3) to 2.175(2) Å, while the corresponding Zn2–N values are in the range from 2.025(2) to 2.030(2) Å, which is in close agreement with the corresponding bond distances of [Zn₅Cl₄(Me₂bta)₆].2DMF (compound **2**),²⁰ with values of 2.183(7) Å (Zn1–N1) and 2.024(5) Å (Zn2–N2). The Zn2–N distances of the tetrahedrally coordinated zinc centres are not much affected by the type of metal atom that is placed in the octahedral coordination site nor by the type of triazolate ligand, as can be deduced from the similar Zn1–N distance found in compound **1** (2.000(2) Å) and the Zn2–N distances in compound **3** (2.025(2)–2.030(2) Å), respectively.

Packing diagrams of compounds **1** and **3** are shown in Fig. 4 and 5. Although the corresponding Kuratowski-type coordination units have identical *T_d* point group symmetry (see Fig. 1), different molecular volumes and shapes of the coordination units give rise to different crystal packing arrangements in **1** and **3**. The [Zn₅Cl₄(ta)₆] unit of the latter compound has a compact, almost spherical shape, and thus its crystal structure consists of closely packed entities. Owing to a less compact shape, compound **1**,

**Fig. 4** Packing plot of compound **1**. Hydrogen atoms and disordered occluded DMF molecules are omitted for clarity.

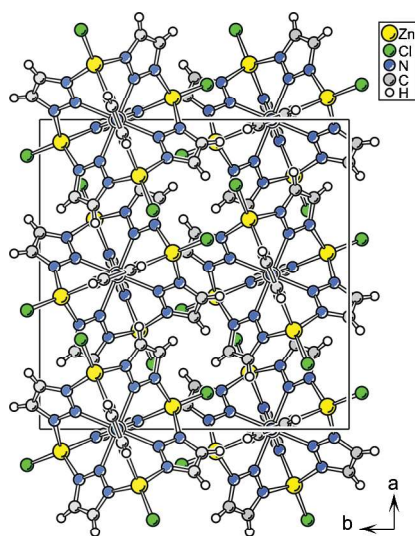


Fig. 5 Packing plot of compound 3.

on the other hand, reveals large voids in its crystal packing arrangement, which are filled by solvent molecules.

UV-vis absorption spectroscopy

The UV-vis absorption spectra of compounds **1** and **3** (recorded from solution) are presented in Fig. 6 and 7; the absorption spectra of compound **2** and of Me₂btaH and taH are included for comparison.

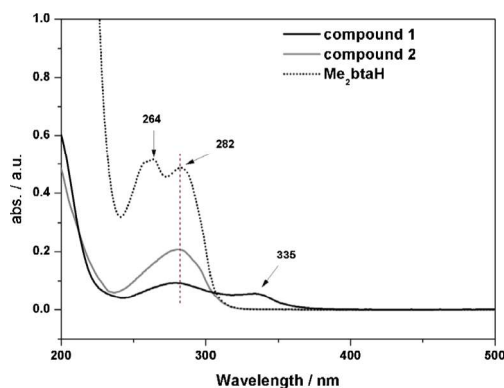


Fig. 6 UV-vis absorption spectra of compounds **1**, **2**, and Me₂btaH recorded from acetonitrile solutions at room temperature (solution conc.: **1** & **2**: 3.25×10^{-7} M; Me₂btaH: 1.95×10^{-6} M).

As shown in Fig. 6, the ligand Me₂btaH shows two adsorption bands in the UV region (282 and 264 nm), whereas this spectral region contains a single band for the corresponding metal complexes, **1** and **2**, centred at 282 nm. According to literature data this relatively intense band can be assigned to the ligand centred $\pi \rightarrow \pi^*$ transitions of Me₂btaH.^{36–38} Compound **1** shows a distinct absorption band near the vis region centred at 335 nm, which is attributed to a Ru^{II} metal-to-ligand charge transfer (MLCT) transition. Electronic transitions at similar energy levels were previously reported for Ru complexes.^{14,39} Compound **2** in contrast shows only one peak in this spectral interval.

For compound **3**, UV-vis absorption spectra were recorded from a methanol solution for both the complex and the ligand. The

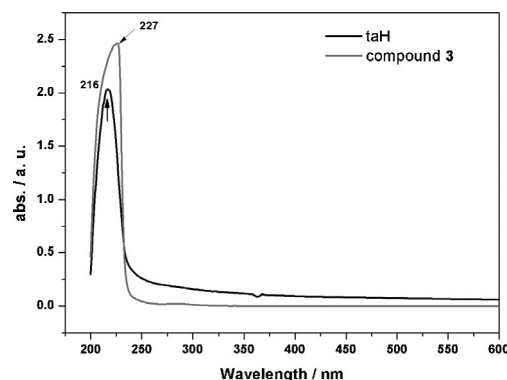


Fig. 7 UV-vis absorption spectra of compound **3** and taH recorded from methanol solution at room temperature (solution conc.: **3**: 6.50×10^{-5} M; taH: 3.90×10^{-4} M).

UV-vis absorption spectra (Fig. 7) exhibit a slight red shift for the metal complex **3** as compared to the free ligand taH. The spectrum of taH is dominated by a band centred at 216 nm arising from $\pi \rightarrow \pi^*$ transitions. When coordinated to zinc ions, the absorption spectrum shows a significant red-shift by approx. 11 nm. This progressive red shift results from the coordination process, which depopulates the electronic aromatic ring of the ligand, increasing the HOMO energy and thus decreasing the HOMO–LUMO gap of the coordination compound with respect to the free ligand. Our calculations give 5.10 eV and 4.36 eV for the HOMO–LUMO gaps in taH and compound **3**, respectively.

FT-IR spectra

The FT-IR spectrum of compound **1** is dominated by a strong absorption at 479 cm^{-1} attributable to a Ru–N bond stretching mode.⁴⁰ The absorption bands at 850 and 1730 cm^{-1} are assigned to out-of-plane deformation vibrations of the C–H bond from the aromatic ring, absorption bands at 1001 and 1197 cm^{-1} are due to the C=C and C–N stretching vibrations respectively, vibrations at 2984 cm^{-1} are attributable to the –CH₃ asymmetric stretching vibration, while the symmetric –CH₃ vibration at 2860 cm^{-1} is also observed. As to compound **3**, absorption bands centred at 811 and 982 cm^{-1} are assigned to C=C stretching vibration, a band at 1187 cm^{-1} is due to the C–H deformation vibration, and =C–H stretching vibration is observed at 3135 cm^{-1} . Further details are given in Fig. S8 and S9 (ESI†).

Computational studies

First-principles calculations were performed in order to study the electronic ground and excited state properties of compounds **1**, **2** and **3**. The subsequent analyses aim at supporting the assignment of certain peaks in the UV-vis and IR spectra and to interpret their components.

Gaussian09⁴¹ and TURBOMOLE V6.1⁴² software codes have been used throughout. DFT was used for geometry optimisations and vibrational analysis, while TDDFT was used to calculate excitation energies, with some few calculations made also with the ZINDO⁴³ method by using the ORCA 2.7 software⁴⁴ Different functionals were tested including B1B95,⁴⁵ B1LYP,^{45,46} B3P86,⁴⁷ B3PW91,⁴⁸ B971,⁴⁹ B972,⁵⁰ BLYP,⁴⁶ BP86,⁵¹ MPW1PW91,⁵² PBE1,⁵³ B98,⁵⁴ VSXC,⁵⁵ B3LYP⁵⁶ and HCTH.⁵⁷ The HCTH

functional was finally chosen as it gave the most balanced accurate results for the properties studied. Def2-basis sets⁵⁸ TZVP, TZVPP and QZVP, from Ahlrich's group were tested and Def2-TZVP was selected for most calculations owing to its very reasonable average accuracy for the properties studied. Geometries of all structural models were optimised obeying full symmetry constraints. Compounds **1**, **2** and **3** were modelled by coordination units shown in Fig. 1 and calculations on free ligands were also considered for the interpretation of UV-vis spectra.

Geometries. The equilibrium geometries (within T_d symmetry) for models of compounds **1**, **2** and **3**, as well as for a (yet to be synthesized) isomer of **3** with $M1 = Ru$ (subsequently labelled **3-Ru**), were optimized with HCTH/Def2-TZVP. Characteristic bond lengths are shown in Table 3, where an atom labelling scheme represented in Fig. 8 is used. When $M1 = Zn$, HCTH calculated Zn1–N1 distances are 2.271 and 2.245 Å for compounds **2** and **3**, which are larger than the experimental values of 2.183(7) Å (**2**) and 2.169(2)–2.175(2) Å (**3**). When $M1 = Ru$, calculated and experimental Ru1–N1 distances for compound **1** are 2.156 and 2.117(3) Å, respectively. As for these and other selected geometric distances (as shown in Table 3), the disagreement between the crystallographic and calculated values is 4% in the worst case (Zn1–N1 distance in **2**), but fall generally within 2% error.

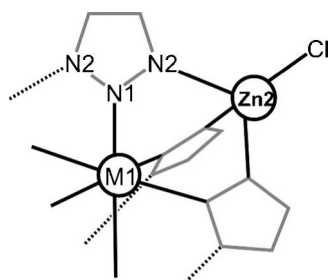


Fig. 8 Different coordination metal ions in Kuratowski-type coordination compounds $[M^II Zn_4 Cl_4 (L)_6]$ ($M^II = Zn$ or Ru , $L^- = Me_2bta^-$ or ta^-). The central metal ions (octahedral coordination) are labelled M1 ($M1 = Ru, Zn$), while tetrahedrally coordinated Zn centres are labelled Zn2. The nitrogen atoms coordinated to M1 are labelled N1, those coordinated to Zn2 are labelled N2.

UV-vis Spectra. As a requirement for the choice of an accurate methodology, the spectra of the free ligands (Me_2btaH and taH) as well as compounds **1**, **2** and **3** should be reasonably reproduced. Apart from Me_2btaH , for which our data is shown in Fig. 6, we have also selected $btaH$, as a related molecule from which extensive computational and experimental data is available, for the sake of comparison.

A study by Borin *et al.*⁵⁹ indicates the difficulty of modelling the experimental data for the $btaH$ molecule, which includes a considerable degree of correlation, and suggests that only CASSCF-PT2 calculations may give an accurate picture of the electronic transitions. Based on their calculations Borin *et al.*⁵⁹ have predicted two absorption bands at 245 nm (5.05 eV) and 275 nm (4.48 eV), in good agreement with a gas phase UV study⁶⁰ at 90 °C showing bands at 5.2 and 4.5 eV respectively, assigned to $\pi \rightarrow \pi^*$ transitions. Several functionals have been used in our study of $btaH$ (Fig. S10, ESI†), with HCTH giving the most accurate results (Fig. 9, top), in excellent agreement with

Table 3 Selected geometric parameters. Distances in Å, angles in degrees. See Fig. 1 for the coordination units investigated in the calculations and Fig. 8 for their label schemes

Geom. Parameter	Exp. (2) ^a	Exp. (3) ^b	Calc. (2)	Calc. (3)
M1 = Zn. HCTH/TZVP				
Zn1–N1	2.183(7)	2.169(2)–2.175(2)	2.271	2.245
Zn2–N2	2.024(5)	2.025(2)–2.030(2)	2.081	2.092
N2–Zn2–N2	99.6(2)	98.25(8)–100.26(8)	99.3	98.5
Zn2–Cl	2.174(3)	2.1550(9)	2.209	2.182
N1–N2	1.346(7)	1.334(2)	1.318	1.318
Geom. Parameter	Exp. (1) ^c		Calc. (1)	Calc. (3-Ru) ^d
M1 = Ru. HCTH/TZVP				
Ru1–N1	2.116(3)	—	2.156	2.136
Zn2–N2	2.000(2)	—	2.042	2.055
N2–Zn2–N2	96.80(8)	—	95.7	95.1
Zn1–Cl	2.1649(8)	—	2.201	2.176
N1–N2	1.335(3)	—	1.321	1.321

^a Compound **2**²⁰ ($M1 = Zn$). ^b Compound **3** ($M1 = Zn$). This work. ^c Compound **1** ($M1 = Ru$). This work. ^d Isostructural with compound **3**, but $M1 = Ru$. Referred to as **3-Ru**.

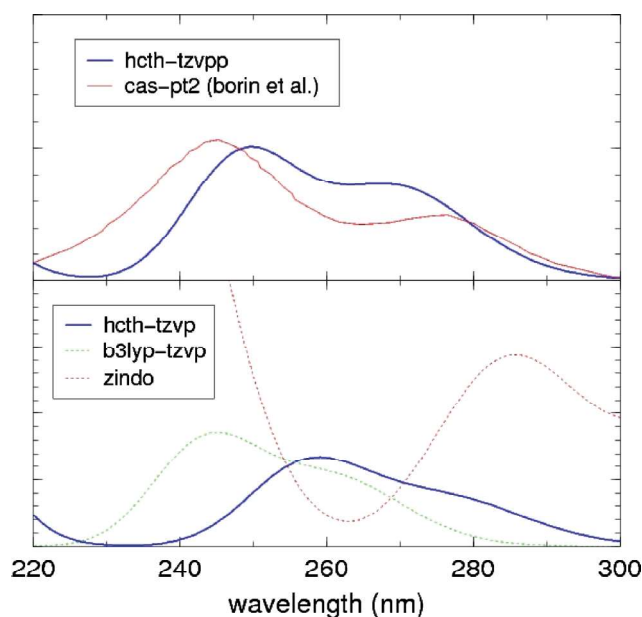


Fig. 9 Calculated UV-vis spectrum of Me_2btaH (5,6-dimethyl-1H-1,2,3-benzotriazole). Top: Comparison of TDDFT (HCTH-TZVPP) vs. the most accurate to date *ab initio* determination from CAS-PT2 by Borin *et al.*⁵⁹ for $btaH$. Bottom: HCTH-TZVP and other less accurate TDDFT (B3LYP/TZVP) and ZINDO calculations of Me_2btaH . TDDFT results for additional methods are shown in Fig. S10, ESI.†

the previous results by Borin *et al.*⁵⁹ and with the experimental measurements by Tomas *et al.*⁶⁰

With TD-DFT/HCTH/Def2-TZVP as our choice, the UV-vis spectrum of Me_2btaH (= ligand of compound **1**) was calculated. Fig. 9 shows the similarity between the TDDFT/HCTH

calculated UV spectra of Me₂btaH (Fig. 9, bottom) and the related molecule btaH (Fig. 9, top). The electron donating methyl groups stabilise the π orbitals by introducing electronic charge, thus increasing the energy of the $\pi \rightarrow \pi^*$ transitions. For Me₂btaH our calculations (Fig. 9, bottom) indicate transitions at 278 and 258 nm, which are in excellent agreement with the observed bands (Fig. 6) at 282 and 264 nm.

The next ligand we studied was taH (= ligand of compound **3**), and the TDDFT/HCTH/Def2-TZVP results (Fig. 10) show a $\pi \rightarrow \pi^*$ transition at 225 nm, in good agreement to the experimentally determined band at 216 nm (Fig. 7).

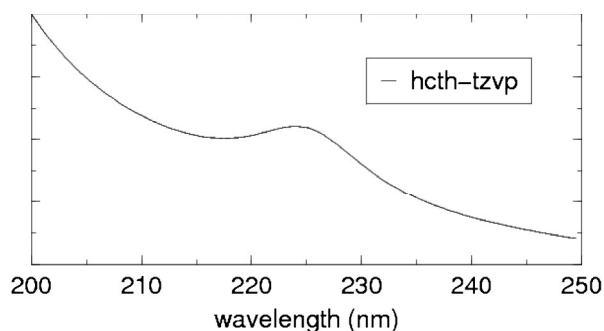


Fig. 10 Calculated UV-vis spectrum of taH (1H-1,2,3-triazole) with TDDFT (HCTH-TZVP), from which an excitation at 225 nm is predicted.

Having obtained consistent computational results for the free ligands, we next attempted to model the UV-vis spectra of compounds **1**, **2** and **3**. TDDFT should model correctly not only the ligands but also the organometallic complexes, which requires a correct treatment of MLCT bands. TDDFT calculations may suffer from the local nature and wrong asymptotic behaviour of approximate functionals, which affect long-range charge transfer (as in some MLCT bands) and high-lying electronic transitions, and in such cases energies of the MLCT bands may become strongly underestimated.

The calculated UV-vis spectra of compound **1** (Fig. 11) required large computational resources due to: (i) the large number of atoms (123) and basis functions (2714), and (ii) the fact that the populated vertical excitations appeared only after the total number of calculated excitations (which increase the computational time

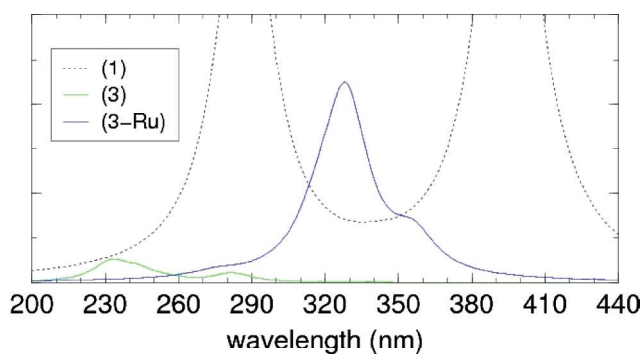


Fig. 11 TDDFT (HCTH-TZVP) calculated UV-vis spectrum of [RuZn₄Cl₄(Me₂bta)₆] (**1**), [Zn₅Cl₄(ta)₆] (**3**) and [RuZn₄Cl₄(ta)₆] (**3-Ru**). 32 excitations have been calculated for (**1**), 70 excitations for (**3**), and 40 excitations for (**3-Ru**).

quadratically) was increased up to 32. Two bands have been found at 395 and 287 nm (Fig. 11), with their respective relative peak intensities being 1.9 and 1.4. A further analysis including the vertical excitations involved in each band is given in Fig. S11, ESI†. It can be seen that the band at higher energy (287 nm) is in excellent agreement with the experimental result of 282 nm (Fig. 6). Our analysis (Fig. S11, ESI†) shows that this calculated band (287 nm) corresponds to a LLCT transition ($\pi \rightarrow \pi^*$) involving the orbitals of the Me₂btaH ligand, which hence appears slightly shifted from that found for the free ligand (calculated at 278 nm in Fig. 9 bottom, and experimentally measured at 282 nm in Fig. 6). The calculated energy-gap (287 nm, 4.3 eV) is extremely close to the experimental value (282 nm, 4.4 eV). On the other hand, the low energy transition calculated at 3.1 eV (395 nm, Fig. 11) appears underestimated with respect to the experimental value of 3.7 eV (335 nm, Fig. 6). The explanation of this shortcoming is the fact that this is a MLCT band that involves moving charge from relatively distant space locations within the large coordination compound **1**, which is a specific and documented source of error in the calculation of electronic excitations with TDDFT methods. Our analysis (Fig. S11, ESI†) shows how the transition involves occupied orbitals mainly localised at the central Ru site whilst the unoccupied orbitals are predominantly localised on the benzene rings of the Me₂btaH ligand. This source of error is expected to be less important in compound **3** due to the absence of the benzene rings and where any MLCT excitation should involve a less drastic spatial charge shift.

Compound **3** has been synthesised containing Zn as the central atom and therefore this means that the UV-vis spectrum, as it is the case for [Zn₅Cl₄(Me₂bta)₆] (**2**), is totally dominated by LLCT transitions, hence with negligible participation of the Zn atoms whose filled d-orbitals lay energetically deep enough so as not to be relevant for the optical spectral features.⁶¹ According to this, a similar UV-vis spectrum is expected for taH and compound **3**, and this is what is experimentally observed in Fig. 7 (bands at 216 and 227 nm respectively). The calculations also show that $\pi \rightarrow \pi^*$ transitions appear at similar wavelength in taH and compound **3**, with the respective values being 225 nm (Fig. 10) and 233 nm (Fig. 11, and see also Fig. S12, ESI† for a more detailed analysis). The agreement between the calculated and experimental values is very good, both for taH (225 nm and 216 nm) and compound **3** (233 nm and 227 nm).

On the other hand, although the Ru-substituted compound **3-Ru** has not been synthesised, it may be interesting to predict how the Ru substitution might influence the UV-vis spectrum. Similar to compound **1**, where the presence of Ru generates a low energy MLCT band, which is absent when the central atom is Zn, the presence of Ru is expected to give a new band arising from electrons located at the Ru-based HOMOs. A weak MLCT band at 357 nm, whose oscillator strength is *ca.* 0.1 has been calculated (Fig. 11), which is due to electrons excited from the occupied frontier orbitals which are localised on the Ru atom. This d \rightarrow d band in **3-Ru** is absent in compound **1** due to the presence, in the latter, of a larger conjugation in the ligands, whose orbitals are higher in energy than the Ru(3d) orbitals. Hence, the HOMO orbitals in compound **3** are mainly due to the ligands, while in **3-Ru** they are mainly due to Ru(3d).

A second stronger band (whose oscillator strength is *ca.* 0.6) appears at 328 nm (Fig. 11), again with MLCT character. This

Table 4 Calculated and experimental main bands of UV-vis spectra

Compound	Calc./nm	Exp./nm	Assign.	Calc./eV	Exp./eV
(3)	233 (Fig. 11)	227 (Fig. 7)	$\pi \rightarrow \pi^*$	5.32	5.46
taH	225 (Fig. 10)	216 (Fig. 7)	$\pi \rightarrow \pi^*$	5.51	5.74
(1)	287 (Fig. 11)	282 (Fig. 6)	$\pi \rightarrow \pi^*$	4.32	4.40
	395 (Fig. 11)	335 (Fig. 6)	MLCT	3.14	3.70
Me ₂ -btaH	258 (Fig. 9)	264 (Fig. 6)	$\pi \rightarrow \pi^*$	4.80	4.70
	278 (Fig. 9)	282 (Fig. 6)	$\pi \rightarrow \pi^*$	4.46	4.40
(3-Ru)	328 (Fig. 11)	N/A	MLCT	3.78	N/A
	357 (Fig. 11)	N/A	d \rightarrow d	3.47	N/A

is further analysed in the ESI (Fig. S13, ESI †). Although the results for (3-Ru) at present can not be compared to experiments, in the case of (1) a discrepancy appears between the calculated and experimental (395 and 335 nm, respectively) MLCT band. CT bands can be poorly predicted by TDDFT when they involve charge transfer between distant parts of the compound. In compound 3-Ru, which is smaller than 1, we can speculate that the systematic error might be smaller.

The differences between the computed values for the main MLCT band in (1) and (3-Ru) (395 and 328 nm respectively) can be rationalized in terms of a larger degree of electronic conjugation effects in compound 1 as compared to compound 3-Ru, since the aromatic benzene rings are not present in the latter. HOMO \rightarrow LUMO transitions are shifted to longer wavelength as the number of conjugated double bonds increases. Our results indicate HOMO–LUMO gaps of 5.10 eV and 3.90 eV for taH and Me₂btaH respectively. For an overall comparison of results Table 4 is given below.

Infrared Spectra. Vibrational calculations have been made within the HCTH/TZVP methodology on compounds 1 and 3 in order to compare calculated values with experimental infrared spectra. A comparison between the experimental and calculated infrared spectra of (1) is shown in Table 5.

The calculated infrared spectrum of (1) shows main features closely related to the experimental results (Table 5).

For compound (3), although the experimental and calculated assignments may differ somehow (see Table 6), the overall shapes of the spectra (Fig. S14 and S8, ESI†) are very similar and we consider this as a reasonable agreement.

The main calculated bands are located at 978, 1138, 1222, 1448, 1485 and 3245 cm⁻¹, whilst the experimental spectrum shows bands, amongst others, at 982, 1130, 1237, 1431, 1459 and 3135 cm⁻¹, and thus the main features look reasonably similar.

Table 5 DFT (HCTH-TZVPP) calculated active normal vibrational modes in the infrared spectra of compound 1. Experimental bands are also indicated

(1) (exp)/cm ⁻¹	Assignment	(1) (calc)/cm ⁻¹
479	RuN stretching	484
850	CH out of plane	867
1001	C=C stretching	1005
1197	CN stretching	1216
	NN stretching	1236
1730	CH out of plane	
2860	CH ₃ symm. stretching	
2984	CH ₃ asymm. stretching	3016

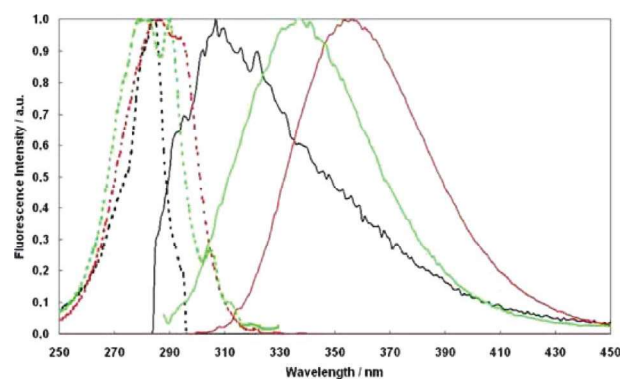
Table 6 DFT (HCTH-TZVPP) calculated active normal vibrational modes in the infrared spectra of compound 3. Selected experimental bands are shown in the first row

(3) (exp)/cm ⁻¹	Assignment	(3) (calc)/cm ⁻¹
811, 982	CH out of plane	815
	C=C stretching	
	ta skeleton, CCN bending	978
	HCN bending	1138
1130	Not assigned	
1187	CH deformation	
	Zn1N asym. stretching	1222
1237	Not assigned	
1431	Not assigned	
	CN stretching or HCN bending	1448
1459	Not assigned	
	C=C stretching	1485
3135	CH stretching	3245

The calculated and experimental Raman spectra of (3) look also quite similar (details are given in Fig. S15 and S9, ESI†). Finally, the infrared spectrum of the Ru-substituted compound 3-Ru is also analysed in the ESI (Figs. S16 and S17†) and its main features are compared to the isostructural compound 3.

Photophysical investigations

Steady state measurements were performed for all three samples: Me₂btaH, compound 1 and 2 dissolved in acetonitrile. Me₂btaH and compound 1 exhibit only very weak fluorescence causing the obtained steady state spectra to be quite noisy. Compound 2 on the other hand emits quite strongly. The respective normalised spectra are shown in Fig. 12.

**Fig. 12** Fluorescence excitation (···) and emission (–) spectra of compound 1 (black), compound 2 (red) and Me₂btaH (green).

While the excitation spectra are found at a similar wavelength range the emission spectra show strong blue shifts (compound 1) and red shifts (compound 2) with respect to the emission of Me₂btaH. The peak positions are summarized in Table 7.

The band at 305 nm of the excitation spectrum of Me₂btaH is caused by the solvent and can be observed when pure acetonitrile is measured under similar conditions (Fig. S18, ESI†). Due to its weak emission, Raman scattering constitutes a serious problem when characterizing especially compound 1. The excitation wavelength had to be shifted far into the blue wing of its absorption spectrum so that the emission is not swamped completely by the Raman signal (Fig. S19, ESI†).

Table 7 Excitation and emission bands of compounds **1** and **2** and Me₂btaH in acetonitrile

Compound	$\lambda_{\text{MAX, EXC.}}$ /nm	$\lambda_{\text{Wing, EXC.}}$ /nm	$\lambda_{\text{MAX, EMI.}}$ /nm	$\lambda_{\text{Wing, EMI.}}$ /nm	QY/%
Me ₂ btaH	281, 290, 305	350	337		1.9
1	284	280/275	307	—	1.8
1 (quasi-steady state)	273		345		
2	287	295	356		68.4

In order to get more reliable data without impeding Raman contribution, a TRES measurement of compound **1** was performed and from these data a quasi steady-state spectrum constructed. If TRES data are integrated for long lifetimes only, the extremely short lived Raman scattering does not contribute to the quasi steady-state spectrum, even if it is present at the respective detection wavelength. The TRES and the quasi steady state spectra are shown in Fig. S20 and S21, ESI†, where it seems that excitation in the red wing of the absorption spectrum leads to an emission band centred at 350 nm. Several emitting species are present in this sample, and a more detailed investigation may be needed to clarify the origin of that band.

When comparing the excitation spectra with the respective absorption bands it is observed, that the absorption band at roughly 282 nm is reflected in all three excitation spectra due to $\pi \rightarrow \pi^*$ transitions of Me₂btaH.

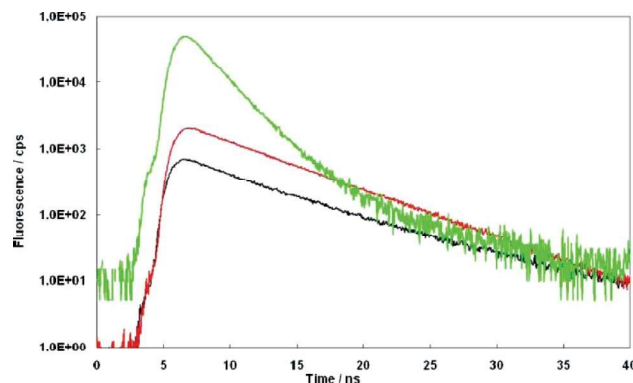
In the case of compound **1** a second absorption band is visible at 335 nm (see Fig. 6) which, according to our calculations (Table 4) is a MLCT band. Excitation of this band allowed the observation of an emission signal between 380 nm and 440 nm (Fig. S22, ESI†). This will be treated in more detail later, when the powdered sample is considered.

Steady-state emission spectra showed that Me₂btaH and compound **1** exhibit only very weak fluorescence while compound **2** shows a strong fluorescence signal. To quantify these differences in fluorescence emission, their respective quantum yields were measured. All three samples were compared to the standard fluorescein, which has a quantum yield of 0.92.⁶² It can be observed (Table 7), that Me₂btaH and compound **1** are practically non-fluorescent while compound **2** has a very high quantum yield of nearly 70%. These findings should be reflected in the fluorescence lifetimes as well (Fig. 13). Compound **2** is expected to have a longer fluorescence lifetime or otherwise no eminent short lived states compared to the other two samples. Lifetime measurements were performed using a pulsed 270 nm LED as excitation light source for all three samples. Results are listed in Table 8.

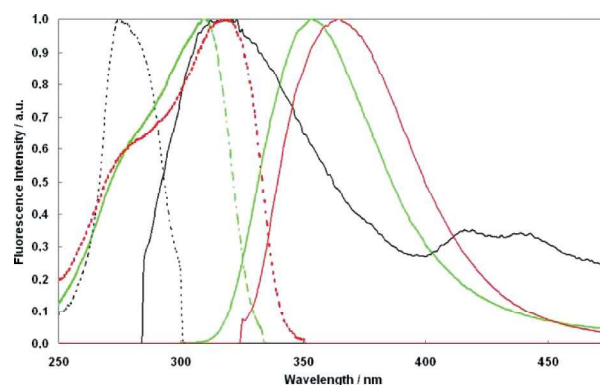
As expected, the long lifetime of 6.05 ns is, in compound **2**, practically the only emitting species, while in Me₂btaH the short lived species with a lifetime of 1.73 ns is predominant.

Table 8 Lifetimes of compounds **1** and **2** and Me₂btaH in acetonitrile

Compound	τ_1 /ns	a_1 /%	τ_2 /ns	a_2 /%	χ^2
Me ₂ btaH	1.73	93.66	5.04	6.34	1.069
1	2.90	20.63	7.61	79.37	0.974
2	2.11	3.1	6.05	96.9	1.122

**Fig. 13** Lifetime measurements of compound **1** (black), compound **2** (red) and Me₂btaH (green).

Owing to the fact that metal complexes show very different properties in different environments, further investigations were done for the samples not in solution but in powdered form. These experiments showed that all three samples show large shifts in their excitation and emission spectra as well as new fluorescence decay components. Fluorescence and excitation spectra are shown in Fig. 14.

**Fig. 14** Fluorescence excitation (···) and emission (—) spectra of compound **1** (black), compound **2** (red) and Me₂btaH (green) investigated as powders.

While the excitation spectra are found in a limited wavelength range the emission spectra show strong blue shifts (compound **1**) and red shifts (compound **2**) with respect to the emission of Me₂btaH. The peak positions are summarized in Table 9.

Compared to the spectra recorded from solution, the emission in the powdered sample is red shifted by 16 nm for Me₂btaH, 11 nm (from 307 to 318 nm) for compound **1**, and 9 nm for compound **2** (from 356 to 365 nm). In the case of compound **1**, additional bands at 415 nm and 440 nm can be observed in the solid sample. This is

Table 9 Excitation and emission bands of compounds **1** and **2** and Me₂btaH investigated as powders

Compound	$\lambda_{\text{MAX, EXC.}}$ /nm	$\lambda_{\text{Wing, EXC.}}$ /nm	$\lambda_{\text{MAX, EMI.}}$ /nm
Me ₂ btaH	309	275	353
1	275	285	317, 415, 440
1 (quasi-steady state)	273		380, 440
2	318	275	365

the same band observed between 380 and 440 nm in solution (Fig. S22, ESI†), which comes from the excitation of the band at 335 nm (see Fig. 6) and is a MLCT band. A TRES was also performed for data slicing purposes to remove the Raman signal. After spectrally correcting the resulting curve, the spectrum in Fig. 15 is produced.

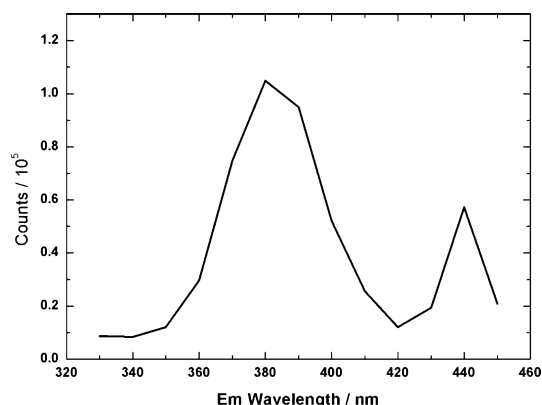


Fig. 15 Gated quasy steady state corrected spectrum of compound **1** with 273 nm excitation.

The respective excitation spectra show quite different behaviour if compared to those gained from dissolved samples: while the excitation bands of Me₂btaH and compound **2** are red shifted, the excitation spectrum of compound **1** peaks now at 275 nm (blue shift by 9 nm). The lifetimes of all three samples in powdered form are listed in Table 10.

Here again compound **1** behaves quite differently than compound **2** and Me₂btaH: while for the latter two samples their lifetimes in solid form are shortened with respect to their lifetimes in acetonitrile, compound **1** exhibits lifetimes an order of magnitude longer than in solution, the main component being 17.4 μs with an amplitude of *ca.* 80%. We suggest this long lifetime is due to the presence of a triplet state. The triplet state could be populated by an intersystem crossing (ISC) with the first excited singlet. Two excited singlets (bands at 282 and 335 nm in Fig. 6) are present in compound **1**, and it is suggested that also a deactivation mechanism S₂→S₁ exists. Therefore the S₁→T₁ ISC can be observed by excitation from the ground state to any of the two excited singlets, and indeed the triplet state has been populated through the 335 nm excitation, S₀→S₁, (in solution, Fig. S22, ESI†), and through the 273 nm excitation, S₀→S₂, (in powdered, Fig. 15). This explains the low quantum yield of fluorescence in compound **1**, and also that the long lifetime of the excited state is only observed in powdered form. A scheme is proposed in Fig. 16.

It is not unusual that octahedral Ru^{II} complexes show a delayed fluorescence (luminescence). A largely studied topic is that of polypyridine derived organometallic complexes, such as the archetype [Ru(bipyridine)₃]²⁺. A triplet LC or MLCT state (with a geometry not far from that of the ground state) is electronically

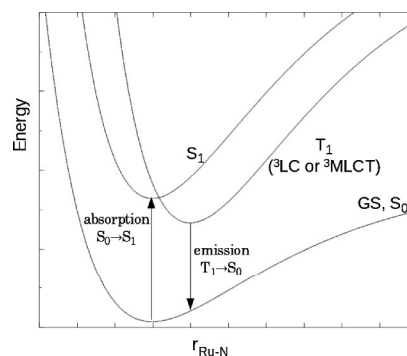


Fig. 16 Proposed scheme showing the states of compound **1**. The transition S₀→S₁ would correspond to the 335 nm band (Fig. 6) which is a MLCT band (Table 4). The transition S₀→S₂ (π→π*, not shown in the scheme) would be the 282 nm band (Fig. 6) which is a LLCT band, from which an internal conversion S₂→S₁ occurs. An intersystem crossing from S₁ to T₁ populates the triplet, from which phosphorescence is observed.

populated upon excitation. The triplet states show large lifetime (in rigid matrix) and hence luminescence is observed.⁶³

Conclusions

Several structurally similar Kuratowski-type coordination compounds have been synthesised and their photophysical properties were investigated. Placing different metal atoms (Ru or Zn) into the central octahedral coordination site, as well as the appropriate selection of the ligand (Me₂btaH or taH) affects the composition and energetic levels of the molecular orbitals in a predictable way, as revealed by interpretation of the electronic absorption spectra supported by the present TDDFT computational study.

As essential features, the relative energies of the frontier molecular orbitals (MO) of the central metal and the ligand determines the type and energy of the allowed transitions. The increasing degree of conjugation (from taH to Me₂btaH) raises the HOMO energies of the donor ligands thus decreasing the bandgap and displacing the transitions towards longer wavelengths. A prominent role of the ligand becomes apparent in the only case here in which LLCT bands have been observed, in compound **3**, where Cl[−] and ta[−] ligands are the main component of the HOMO and LUMO orbitals, respectively. The somewhat atypical role of the Cl[−] ligands as the main contributors of the HOMO is due to the absence of otherwise higher HOMO energies if Ru, as the central atom (instead of Zn), or Me₂bta[−], as the ligand (instead of ta[−]), were present. Therefore, this contributes to the high excitation energies, and compound **3** shows the largest bandgap of all the studied complexes.

In compound **1**, in contrast, there is a good overlap between the LUMO (mainly from Ru) and HOMO (mainly from N=N π orbitals from Me₂bta[−]), giving a small HOMO–LUMO bandgap (Fig. S11†). All this contributes to a MLCT band that is equally intense as that, at higher energy, coming from the π→π* transition (LLCT) of the ligand Me₂btaH. These two bands correspond to the states S₀→S₁ and S₀→S₂ respectively. The excitation of both bands leads to the population of what we believe is a triplet state through an intersystem crossing S₁→T₁, which (in powdered form) is responsible for the long-lived excited state with a lifetime of *ca.* 17 μs.

Table 10 Lifetimes of compounds **1**, **2** and Me₂btaH (powders)

Sample	τ ₁ /nm	a ₁ /%	τ ₂ /nm	a ₂ /%	τ ₃ /nm	a ₃ /%	χ ²
Me ₂ btaH	0.23	16.33	1.08	83.67			1.264
1	316.70	2.72	2350	17.56	17400	79.72	1.005
2	0.14	9.76	2.65	88.00	6.57	2.24	1.106

Based on the combined photophysical and theoretical investigations it is tempting to suggest the construction of solid state compounds (*i.e.* metal–organic frameworks) featuring Kuratowski-type secondary building units of the kind presented in the present publication. Doping MOFs such as MFU-4 with Ru centres might thus lead to potent photocatalysts, which could make use of the high photon collecting efficiency (*i.e.* quantum yield) of the zinc-only containing SBUs (as exemplified for compound **2**), which in turn might show energy or electron transfer to (excited) Ru-containing SBUs (as represented by compound **3**), the latter being excellent candidates for photocatalytically active centres, owing to their long-lived photoexcited electronic state. Investigations in this direction are currently being undertaken in our laboratories.

Experimental

Materials and general methods

Unless noted otherwise, all manipulations were carried out in an argon atmosphere by means of standard Schlenk techniques. The precursor species *trans*-Ru(DMSO)₄Cl₂³³ and [Ru(MeCN)₆][ZnCl₄]·2.5H₂O³⁴ were prepared according to the published procedure. Methanol was distilled from magnesium prior to use. Acetonitrile and NMP used for spectroscopic studies were commercially available in spectroscopic grade. All other starting materials were commercially available reagents of analytical grade and used without further purification.

Fourier transform infrared (FTIR) spectra were recorded in the region of 400–4000 cm^{−1} in Nujol on a Bruker IFS FTIR spectrometer. Elemental analyses (C, H, N) were carried out on a Perkin-55 Elmer 2400 Elemental Analyzer. Metal determinations were carried out on Thermo ICAF ICP-AES (inductively coupled plasma atomic emission spectroscopy) after treatment with HNO₃/HCl under pressure at 180 °C at the Mikroanalytisches Labor Pascher, Remagen, Germany. Thermogravimetric analysis (TGA) was performed with a TGA/SDTA851 Mettler Toledo analyzer in the temperature range of 25–1100 °C at a heating rate of 10 °C min^{−1} in nitrogen flow. UV-vis spectra of compound **1** and compound **2**, as well as of the Me₂btaH ligand were recorded on a Perkin-Elmer Lambda 19 UV-vis spectrometer in the range of 200–900 nm; spectra of compound **3** and the taH ligand were recorded on an Analytik Jena Specord UV-vis spectrometer in the range of 200–1000 nm with a lamp change at 320 nm. Compound **3** with poor solubility was uniformly suspended in methanol solution *via* ultrasound treatment for 10 min, the even suspension was transferred to a 10 mm path length quartz cuvette where the data was recorded. All other samples were dissolved in solution and measured at room temperature. X-Ray powder diffraction (XRPD) patterns were measured using a Panalytical X'Pert Pro powder diffractometer operated at 40 kV, 40 mA for Cu-Kα (λ = 1.5406 Å) with a scan speed of 30 s × step^{−1} and a step size of 0.008°. LIFDI-MS spectra was measured on JEOL JMS-T100GCV equipped with a LIFDI ionization source, operated at a cathode voltage of −10 kV (emitter current control: 0–80 mA, 25.6 mA min^{−1}).

Synthesis of [Ru^{II}Zn₄Cl₄(C₈H₈N₃)₆]-2C₃H₇NO (**1**)

Method 1: step by step synthesis.

Step 1. Synthesis of the precursor complex Ru(Me₂btaH)₆Cl₂. 0.1 g of *trans*-Ru(DMSO)₄Cl₂ and 1.365 g of Me₂btaH (melting point: 153–156 °C) were mixed in solid state and heated to 170 °C until the ligand was fully melted. The reaction mixture was stirred at this temperature for 5 h, then cooled to room temperature and 50 mL of degassed acetone was added to dissolve the unreacted ligand. A light yellow powder (mixture **1a**) was collected by filtration, washed thoroughly with acetone and dried.

Step 2. Synthesis of [Ru^{II}Zn₄Cl₄(C₈H₈N₃)₆]-2C₃H₇NO (1**).** Solvothermal method: Mixture **1a** (0.029 g) was dissolved in 4 mL DMF and heated to 100 °C until fully dissolved, then ZnCl₂ (0.015 g) was added and the solution was placed in a small pyrex tube, sealed and heated to 120 °C. After holding at this temperature for 2h, the solution slowly changed from greenish yellow to reddish orange. The mixture was then cooled to room temperature and greenish yellow octahedral crystals were collected by filtration, washed with 2 × 3 mL DMF and vacuum dried. Yield: 0.010 g, 26% (based on ZnCl₂). Elemental analysis for H₆₂C₅₄N₂₀O₂Cl₄Zn₄Ru: calcd C 42.46, H 4.09, N 18.34 (%); found C 42.56, H 4.15, N 18.40 (%). ICP-AES for the content of metal ions: calcd Ru 6.62, Zn 17.12 (%); found Ru 6.82, Zn 17.05 (%). ¹H NMR (400 MHz, bromobenzene-*d*₅, 25 °C, ppm): δ = 8.73 (s, 12H, PhH), 8.08 (s, 2H, CHO), 2.84 (s, 6H, CH₃), 2.64 (s, 6H, CH₃), 2.46 (s, 36H, CH₃). LIFDI-MS (ethyl acetate): *m/z* for H₄₈C₄₈N₁₈Cl₄Zn₄Ru ([1-2DMF]) calcd 1381.5, found 1381.9. IR (KBr, cm^{−1}): 438 (w), 479 (m), 502 (w), 583 (w), 656 (w), 697 (w), 724 (w), 850 (vs), 1001 (s), 1027 (s), 1068 (s), 1083 (sh), 1167 (w), 1197 (vs), 1255 (w), 1311 (s), 1377 (s), 1454 (vs), 1494 (s), 1578 (s), 1730 (vs), 2380 (w), 2731 (w), 2860 (br), 2923 (w), 2948 (w), 2984 (m), 3054 (w), 3430 (br).

Diffusion method: Mixture **1a** (0.029 g) was dissolved in 3 mL DMF and heated to 100 °C until fully dissolved, then ZnCl₂ (0.015 g) was added into and resulted in a greenish yellow solution, which was placed in a small vial (10 mL). The vial was then placed in a larger vial (45 mL) containing 8 mL DMF and 50 μL TEA. The large vial was sealed and left undisturbed for 1 week to allow the TEA to slowly diffuse into the small vial. Light yellow octahedral crystals were grown from the greenish yellow solution, collected by filtration and washed with 2 × 3 mL DMF and vacuum dried. Yield: 2 mg, 5% (based on ZnCl₂).

Method 2: direct synthesis. [Ru(MeCN)₆][ZnCl₄]·2.5H₂O (0.03 g, 0.05 mmol) was dissolved in 3 mL of DMF, followed by the addition of the Me₂btaH ligand (0.044 g, 0.3 mmol) and ZnCl₂ (0.02 g, 0.15 mmol). The solution was placed in a 15 mL pyrex tube, sealed and heated to 120 °C and held at that temperature overnight, then cooled to room temperature. Greenish yellow octahedral crystals were collected by filtration, washed with 2 × 3 mL DMF and vacuum dried. Yield: 0.01 g, 16%. Elemental analysis for H₆₂C₅₄N₂₀O₂Cl₄Zn₄Ru: calcd C 42.46, H 4.09, N 18.34 (%); found C 42.23, H 4.09, N 18.12 (%). ICP-MS for the content of metal ions: calcd Ru 6.62, Zn 17.12 (%); found Ru 6.79, Zn 16.80 (%). ¹H NMR (400 MHz, bromobenzene-*d*₅, 25 °C, ppm): δ = 8.73 (s, 12H, PhH), 8.08 (s, 2H, CHO), 2.84 (s, 6H, CH₃), 2.65 (s, 6H, CH₃), 2.47 (s, 36H, CH₃).

Synthesis of Zn₅Cl₄(C₂H₂N₃)₆ (**3**)

Method 1: solvothermal synthesis. ZnCl₂ (0.0136 g, 0.1 mmol) and 1*H*-1,2,3-triazole (0.0261 mL, 0.45 mmol) were dissolved in 4 mL of butanol. The solution was placed in a 15 mL pyrex tube,

sealed and heated to 130 °C and held at that temperature for 2 d, then cooled to room temperature. The colourless crystal were collected and washed with 2 × 3 mL of methanol and vacuum dried. Yield: 6 mg, 34%. Elemental analysis for $\text{H}_{12}\text{C}_{12}\text{N}_{18}\text{Cl}_4\text{Zn}_3$: calcd C 16.43, H 1.38, N 28.74 (%); found C 16.24, H 1.41, N 24.36(%). IR (KBr, cm^{-1}): 627 (w), 713 (w), 811 (s), 982 (s), 1010 (w), 1130 (s), 1187 (s), 1237 (w), 1431 (w), 1459 (m), 1611 (w), 1676 (w), 1759 (w), 2228 (w), 2462 (w), 2924 (w), 3135 (m), 3420 (br), 3666 (w), 3790 (w), 3945 (w).

Method 2: microwave assisted synthesis. ZnCl_2 (0.0136 g, 0.1 mmol) and 1*H*-1,2,3-triazole (0.0261 mL, 0.45 mmol) were dissolved in 3 mL of butanol, the solution was placed in pyrex sample tube (10 mL), sealed and transferred into a microwave synthesizer. The reaction parameter was set at 150 W, heated to 160 °C and held at that temperature for 15 min, then cooled to room temperature. The colourless crystals were collected and washed with 2 × 3 mL of methanol and vacuum dried. Yield: 4 mg, 23%.

Crystallographic structure determination

A summary of the detailed single crystal data collection and refinement of compounds **1** and **3** are reported in Table 2. The data of compounds **1** and **3** were collected on a STOE IPDS diffractometer employing monochromated Mo-K α radiation ($\lambda = 0.71073$). The structures were solved by direct methods with additional light atoms found by Fourier methods and refined by full-matrix least-squares techniques based on F^2 using the SHELXL-97 program.⁶⁴ Anisotropic displacement parameters were used for all non H-atoms. Hydrogen atoms were added at calculated positions. H-atoms were given isotropic displacement parameters equal to 1.2 times the equivalent isotropic displacement parameter of the atom to which the H-atom was attached. Semi-empirical absorption correction was applied using multi-scan absorption correction⁶⁵ for compound **1** ($T_{\min} = 0.5563$, $T_{\max} = 0.5947$) and compound **3** ($T_{\min} = 0.2610$, $T_{\max} = 0.6184$).⁶⁶ The crystallographic data for the structure reported in this paper are available as CCDC 804602 (compound **1**) and CCDC 804603 (compound **3**).†

Photophysical Measurements

Steady-state fluorescence spectra were recorded in a spectral range from 200 to 870 nm on an Edinburgh Instruments' FLS920 Spectrometer with double monochromators in excitation and emission light path, a TE Cooled R928P PMT and a 450 W Xenon lamp. For fluorescence lifetime measurements this system was equipped with a pulsed LED for excitation at 270 nm and a diode laser for excitation at 375 nm. Concentration of samples in fluorescence measurements: all samples were dissolved in acetonitrile solution and the solutions were diluted until the appropriate concentration regime was reached that matched the (linear) absorption range of the fluorescence spectrometer.

Acknowledgements

Financial support from the German Research Foundation (DFG Priority Program 1362 "Porous Metal–Organic Frameworks", VO 829/5-1) is gratefully acknowledged. M.T. is grateful to the Landesgraduiertenförderung Baden-Württemberg for financial

support. GS thanks Ministerio de Ciencia e Innovacion of Spain for funding through project MAT2007-64682. BSC (Barcelona Supercomputing Centre) is thanked for providing computer resources. Helpful discussions with Dr Virginie Lhiaubet are gratefully acknowledged.

Notes and references

- 1 R. S. Shaw, R. H. Laye, L. F. Jones, D. M. Low, C. Talbot-Eeckelaers, Q. Wei, C. J. Milios, S. Teat, M. Helliwell, J. Raftery, M. Evangelisti, M. Affronte, D. Collison, E. K. Brechin and E. J. L. McInnes, *Inorg. Chem.*, 2007, **46**, 4968–4978.
- 2 S. M. Tekarli, T. R. Cundari and M. A. Omary, *J. Am. Chem. Soc.*, 2008, **130**, 1669–1675.
- 3 J.-P. Zhang, Y.-Y. Lin, X.-C. Huang and X.-M. Chen, *J. Am. Chem. Soc.*, 2005, **127**, 5495–5506.
- 4 R. C. Rocha and H. E. Toma, *Polyhedron*, 2003, **22**, 1303–1313.
- 5 R. C. Rocha, F. N. Rein, H. Jude, A. P. Shreve, J. J. Concepcion and T. J. Meyer, *Angew. Chem., Int. Ed.*, 2008, **47**, 503–506.
- 6 H. Struthers, B. Spingler, T. L. Mindt and R. Schibli, *Chem.–Eur. J.*, 2008, **14**, 6173–6183.
- 7 F. E. Jernigan Iii, N. A. Sieracki, M. T. Taylor, A. S. Jenkins, S. E. Engel, B. W. Rowe, F. A. Jové, G. P. A. Yap, E. T. Papish and G. M. Ferrence, *Inorg. Chem.*, 2007, **46**, 360–362.
- 8 S. Ferrer, R. Ballesteros, A. Sambartolomé, M. González, G. Alzueta, J. Borrás and M. Liu, *J. Inorg. Biochem.*, 2004, **98**, 1436–1446.
- 9 M. Obata, A. Kitamura, A. Mori, C. Kameyama, J. A. Czaplewskia, R. Tanaka, I. Kinoshita, T. Kusumoto, H. Hashimoto, M. Harada, Y. Mikata, T. Funabiki and S. Yano, *Dalton Trans.*, 2008, 3292–3300.
- 10 D. Schweinfurth, R. Pattacini, S. Strobel and B. Sarkar, *Dalton Trans.*, 2009, 9291–9297.
- 11 K. T. Potts, *Chem. Rev.*, 1961, **61**, 87–127.
- 12 C. Richardson and P. J. Steel, *Dalton Trans.*, 2003, 992–1000.
- 13 R. C. Rocha and H. E. Toma, *Transition Met. Chem.*, 2003, **28**, 43–50.
- 14 R. C. Rocha and H. E. Toma, *Inorg. Chim. Acta*, 2000, **310**, 65–80.
- 15 R. C. Rocha and H. E. Toma, *Polyhedron*, 2002, **21**, 2089–2098.
- 16 M. Obata, A. Kitamura, A. Mori, C. Kameyama, J. A. Czaplewskia, R. Tanaka, I. Kinoshita, T. Kusumoto, H. Hashimoto, M. Harada, Y. Mikata, T. Funabiki and S. Yano, *Dalton Trans.*, 2008, 3292–3300.
- 17 M. Felici, P. Contreras-Carballada, Y. Vida, J. M. M. Smits, R. J. M. Nolte, L. De Cola, R. M. Williams and M. C. Feiters, *Chem.–Eur. J.*, 2009, **15**, 13124–13134.
- 18 B. Schulze, C. Friebe, M. D. Hager, A. Winter, R. Hoogenboom, H. Görls and U. S. Schubert, *Dalton Trans.*, 2009, 787–794.
- 19 S. Biswas, M. Tonigold, M. Speldrich, P. Kögerler, M. Weil and D. Volkmer, *Inorg. Chem.*, 2010, **49**, 7424–7434.
- 20 S. Biswas, M. Tonigold and D. Volkmer, *Z. Anorg. Allg. Chem.*, 2008, **634**, 2532–2538.
- 21 Y.-X. Yuan, P.-J. Wei, W. Qin, Y. Zhang, J.-L. Yao and R.-A. Gu, *Eur. J. Inorg. Chem.*, 2007, 4980–4987.
- 22 Y.-L. Bai, J. Tao, R.-B. Huang and L.-S. Zheng, *Angew. Chem., Int. Ed.*, 2008, **47**, 5344–5347.
- 23 J. Handley, D. Collison, C. D. Garner, M. Helliwell, R. Docherty, J. R. Lawson and P. A. Tasker, *Angew. Chem., Int. Ed. Engl.*, 1993, **32**, 1036–1038.
- 24 M. Murrie, D. Collison, C. D. Garner, M. Helliwell, P. A. Tasker and S. S. Turner, *Polyhedron*, 1998, **17**, 3031–3043.
- 25 G. F. Kokoszka, J. Baranowski, C. Goldstein, J. Orsini, A. D. Mighell, V. L. Himes and A. R. Siedle, *J. Am. Chem. Soc.*, 1983, **105**, 5627–5633.
- 26 S. Biswas, M. Grzywa, H. P. Nayek, S. Dehnen, I. Senkovska, S. Kaskel and D. Volkmer, *Dalton Trans.*, 2009, 6487–6495.
- 27 D. Denysenko, M. Grzywa, M. Tonigold, B. Schmitz, I. Krkljus, M. Hirscher, E. Mugnaioli, U. Kolb, J. Hanss and D. Volkmer, *Chem. Eur. J.*, 2011, **17**, 1837–1848.
- 28 C. Kuratowski, *Fund. Mat.*, 1930, **15**, 271–283.
- 29 S. Biswas, M. Tonigold, M. Speldrich, P. Kögerler and D. Volkmer, *Eur. J. Inorg. Chem.*, 2009, 3094–3101.
- 30 S. Biswas, M. Tonigold, H. Kelm, H.-J. Krüger and D. Volkmer, *Dalton Trans.*, 2010, **39**, 9851–9859.
- 31 X. L. Wang, C. Qin, S. X. Wu, K. Z. Shao, Y. Q. Lan, S. Wang, D. X. Zhu, Z. M. Su and E. B. Wang, *Angew. Chem., Int. Ed.*, 2009, **48**, 5291–5295.

- 32 A. Vlček Jr and S. Zálaiš, *Coord. Chem. Rev.*, 2007, **251**, 258–287.
- 33 I. P. Evans, A. Spencer and G. Wilkinson, *J. Chem. Soc., Dalton Trans.*, 1973, 204–209.
- 34 A. Anzellotti and A. Briceno, *Acta Crystallogr., Sect. E: Struct. Rep. Online*, 2001, **57**, m538–m540.
- 35 E. Reisner, V. B. Arion, A. Rufinska, I. Chiorescu, W. F. Schmid and B. K. Keppler, *Dalton Trans.*, 2005, 2355–2364.
- 36 M. Duati, S. Tasca, F. C. Lynch, H. Bohlen, J. G. Vos, S. Stagni and M. D. Ward, *Inorg. Chem.*, 2003, **42**, 8377–8384.
- 37 S. Stagni, E. Orselli, A. Palazzi, L. De Cola, S. Zacchini, C. Femoni, M. Marcaccio, F. Paolucci and S. Zanarini, *Inorg. Chem.*, 2007, **46**, 9126–9138.
- 38 G. Giuffrida, G. Calogero, G. Guglielmo, V. Ricevuto, M. Ciano and S. Campagna, *Inorg. Chem.*, 1993, **32**, 1179–1183.
- 39 K. Araki, F. N. Rein, S. G. Camera and H. E. Toma, *Transition Met. Chem.*, 1992, **17**, 535–538.
- 40 E. Alessio, G. Balducci, A. Lutman, G. Mestroni, M. Calligaris and W. M. Attia, *Inorg. Chim. Acta*, 1993, **203**, 205–217.
- 41 M. J. Frisch, G. W. Trucks, H. B. Schlegel, G. E. Scuseria, M. A. Robb, J. R. Cheeseman, G. Scalmani, V. Barone, B. Mennucci, G. A. Petersson, H. Nakatsuji, M. Caricato, X. Li, H. P. Hratchian, A. F. Izmaylov, J. Bloino, G. Zheng, J. L. Sonnenberg, M. Hada, M. Ehara, K. Toyota, R. Fukuda, J. Hasegawa, M. Ishida, T. Nakajima, Y. Honda, O. Kitao, H. Nakai, T. Vreven, J. A. Montgomery, Jr., J. E. Peralta, F. Ogliaro, M. Bearpark, J. J. Heyd, E. Brothers, K. N. Kudin, V. N. Staroverov, R. Kobayashi, J. Normand, K. Raghavachari, A. Rendell, J. C. Burant, S. S. Iyengar, J. Tomasi, M. Cossi, N. Rega, J. M. Millam, M. Klene, J. E. Knox, J. B. Cross, V. Bakken, C. Adamo, J. Jaramillo, R. Gomperts, R. E. Stratmann, O. Yazyev, A. J. Austin, R. Cammi, C. Pomelli, J. Ochterski, R. L. Martin, K. Morokuma, V. G. Zakrzewski, G. A. Voth, P. Salvador, J. J. Dannenberg, S. Dapprich, A. D. Daniels, O. Farkas, J. B. Foresman, J. V. Ortiz, J. Cioslowski and D. J. Fox, *GAUSSIAN 09 (Revision A.1)*, Gaussian, Inc., Wallingford, CT, 2009.
- 42 R. Ahlrichs, M. Bär, M. Häser, H. Horn and C. Kölmel, *Chem. Phys. Lett.*, 1989, **162**, 165–169.
- 43 (a) W. Thiel and A. A. Voityuk, *Theor. Chim. Acta*, 1992, **81**, 391–404; (b) W. Thiel and A. A. Voityuk, *J. Phys. Chem.*, 1996, **100**, 616–626.
- 44 ORCA 2.7, F. Neese, *ORCA, an ab initio, density functional and semiempirical program package*, University of Bonn, Bonn, Germany, 2007.
- 45 A. D. Becke, *J. Chem. Phys.*, 1996, **104**, 1040–1046.
- 46 C. Lee, W. Yang and R. G. Parr, *Phys. Rev. B*, 1988, **37**, 785–789.
- 47 J. P. Perdew, *Phys. Rev. B*, 1986, **33**, 8822–8824.
- 48 J. P. Perdew, J. A. Chevary, S. H. Vosko, K. A. Jackson, M. R. Pederson, D. J. Singh and C. Fiolhais, *Phys. Rev. B: Condens. Matter*, 1992, **46**, 6671–6687.
- 49 F. A. Hamprecht, A. Cohen, D. J. Tozer and N. C. Handy, *J. Chem. Phys.*, 1998, **109**, 6264–6271.
- 50 P. J. Wilson, T. J. Bradley and D. J. Tozer, *J. Chem. Phys.*, 2001, **115**, 9233–9242.
- 51 A. D. Becke, *Phys. Rev. A: At., Mol., Opt. Phys.*, 1988, **38**, 3098–3100.
- 52 C. Adamo and E. Barone, *J. Chem. Phys.*, 1998, **108**, 664–675.
- 53 C. Adamo and E. Barone, *J. Chem. Phys.*, 1999, **110**, 6158–6169.
- 54 H. L. Schmider and A. D. Becke, *J. Chem. Phys.*, 1998, **108**, 9624–9631.
- 55 T. Van Voorhis and G. E. Scuseria, *J. Chem. Phys.*, 1998, **109**, 400–410.
- 56 A. D. Becke, *J. Chem. Phys.*, 1993, **98**, 1372–1377.
- 57 A. D. Boese and N. C. Handy, *J. Chem. Phys.*, 2001, **114**, 5497–5503.
- 58 (a) F. Weigend and R. Ahlrichs, *Phys. Chem. Chem. Phys.*, 2005, **7**, 3297–3305; (b) A. Schaefer, C. Huber and R. Ahlrichs, *J. Chem. Phys.*, 1994, **100**, 5829–5835; (c) K. Eichkorn, F. Weigend, O. Treutler and R. Ahlrichs, *Theor. Chem. Acc.*, 1997, **97**, 119–124; (d) F. Weigend, F. Furche and R. Ahlrichs, *J. Chem. Phys.*, 2003, **119**, 12753–12762; (e) D. Andrae, U. Haeussermann, M. Dolg, H. Stoll and H. Preuss, *Theor. Chim. Acta*, 1990, **77**, 123–141.
- 59 A. C. Borin, L. Serrano-Andres, V. Ludwig and S. Canuto, *Phys. Chem. Chem. Phys.*, 2003, **5**, 5001–5009.
- 60 F. Tomas, J. Catalan, P. Perez and J. Elguero, *J. Org. Chem.*, 1994, **59**, 2799.
- 61 Calculated UV-vis absorption spectrum of compound **2** is included as ESI.
- 62 P. G. Seybold, M. Gouterman and J. Callis, *Photochem. Photobiol.*, 1969, **9**, 229–242.
- 63 See pages 121 and 124–125 in: S. Campagna, F. Puntoriero, F. Nastasi, G. Bergamini and V. Balzani, Photochemistry and Photophysics of Coordination Compounds: Ruthenium, *Top. Curr. Chem.*, 2007, **280**, 117–214.
- 64 G. M. Sheldrick, *SHELXL-97, Program for refinement of crystal structures*, University of Göttingen, Germany, 1997.
- 65 R. H. Blessing, *Acta Cryst. A*, 1995, **51**, 33–38.
- 66 A. L. Spek, *J. Appl. Crystallogr.*, 2003, **36**, 7–13.